

**Enhanced Stability of Silicon for Photoelectrochemical Water Oxidation Through Self-Healing Enabled by an Alkaline Protective Electrolyte**

Harold J. Fu<sup>1</sup>, Ivan A. Moreno-Hernandez<sup>1</sup>, Pakpoom Buabthong<sup>2</sup>, Kimberly M. Papadantonakis<sup>1</sup>, Bruce S. Brunschwig<sup>3</sup>, Nathan S. Lewis<sup>1,3</sup>

<sup>1</sup>Division of Chemistry and Chemical Engineering, 127-72, California Institute of Technology, Pasadena, CA 91125, USA

<sup>2</sup>Division of Engineering and Applied Sciences, California Institute of Technology, Pasadena, CA 91125

<sup>3</sup>Beckman Institute Molecular Materials Research Center, California Institute of Technology, Pasadena, CA 91125, USA

\*Correspondence to: [nslewis@caltech.edu](mailto:nslewis@caltech.edu)

## Supplementary Information

### Materials and Methods

#### Chemicals:

All chemicals were used as received, including potassium hydroxide (KOH, Macron Fine Chemicals, NF/FCC grade), potassium ferricyanide ( $\text{K}_3\text{Fe}(\text{CN})_6$ , Fischer Chemical, Certified ACS), potassium ferrocyanide trihydrate ( $\text{K}_4\text{Fe}(\text{CN})_6 \cdot 3\text{H}_2\text{O}$ , Fischer Chemical, Certified ACS), hydrochloric acid (HCl, EMD Millipore Co., 36-38%), hydrogen peroxide ( $\text{H}_2\text{O}_2$ , EMD Millipore Co., 30%), buffered oxide etchant (BOE, 6:1  $\text{NH}_4\text{F}$  to HF, Transene Company, Inc.), and gallium-indium eutectic (Alfa Aesar, 99.99%). Deionized water (18.2  $\text{M}\Omega$  cm resistivity) was obtained from a Barnstead Millipore system.

#### Electrode Preparation:

Both n-type (phosphorous doped, 0.1-1.0  $\Omega$  cm, (100)-oriented) and  $\text{p}^+$ -type (boron doped, 0.001-0.005  $\Omega$  cm, (100)-oriented) Si wafers were purchased from Addison Engineering. Boron diffusion doping was used to create an  $\text{np}^+$  junction on the n-type wafer. Prior to doping, n-type wafers were cleaned by etching in BOE for 30 s followed by immersion in 6 : 1 : 1  $\text{H}_2\text{O}$  : HCl :  $\text{H}_2\text{O}_2$  (by volume) at 75 °C for 15 min. The wafers were then rinsed with deionized water and dried under flowing  $\text{N}_2(\text{g})$ .

The tube furnace used for diffusion doping had an  $\text{O}_2$  flow at 950 °C for 30 min to oxidize boron nitride wafers (Saint-Gobain, BN-975 PDS). The gas supply was switched from  $\text{O}_2$  to  $\text{N}_2$  and the furnace was cooled to 750 °C before inserting cleaned n-type wafers. A  $\text{p}^+$ -

emitter was formed after increasing the temperature back to 950 °C under N<sub>2</sub>, and the temperature was maintained for 30 min. After diffusion doping, the sample was left to cool to room temperature and then submerged in BOE for 2 min to deglaze B<sub>2</sub>O<sub>3</sub> from the surface. Low temperature oxidation at 750 °C under O<sub>2</sub> for 20 min was performed to remove surface defects. The sample was then submerged in BOE until the surface was no longer hydrophilic. A sheet resistance of ~ 40-70 Ω/sq was obtained using a four-point probe (Jandel).

An array of Ni catalyst microelectrodes (μNi), with a 3 μm diameter and 7 μm pitch, was patterned onto Si wafers using photolithography. The Si wafer was rinsed with deionized water and MCC primer 80/20 (Microchem Corp.) was deposited onto the surface via spin coating at 3000 rpm for 1 min. Shipley 1813 photoresist was then coated at 3000 rpm for 1 min and then heated for 1 min at 110 °C. The pattern was exposed to UV light through a chrome mask to define the array. The exposed regions were washed away using MF-319 developer (Microchem Corp.) for 2 min, and were then rinsed with deionized water. The patterned wafer was baked at 110 °C. Prior to Ni deposition, the patterned wafer was etched with BOE for 30 s. The Ni catalyst was deposited using radio-frequency (RF) sputtering with an AJA Orion sputtering system at 100 W for 1 h (Ni target from Kurt J. Lesker Company). The Ar flow rate during sputtering was maintained at 20 sccm to maintain the plasma while the chamber pressure was 5 mTorr. After sputtering, the photoresist of the patterned wafers was removed by submerging the wafer in acetone and gently sonicating for at least 30 min. Unpatterned p<sup>+</sup>-Si wafers for activity and faradaic efficiency measurements had a Ni overlayer similarly deposited using the BOE etch and sputtering steps as described.

Electrodes were fabricated by first cleaving the sample with a carbide scribe to the desired area. Electrodes in contact with [Fe(CN)<sub>6</sub>]<sup>3-</sup> and KOH electrolyte in Fig. 1 had areas

between 10-15 mm<sup>2</sup>, and each run showed similar performance and stability. Wafers that went through either diffusion doping and/or Ni sputtering had their edges cleaved and discarded to prevent shunts during operation. In-Ga eutectic (Ted Pella) was scratched onto the backs of the sample and affixed to a Sn-coated Cu wire using Ag paint (Ted Pella). The wire was threaded through a glass rod and the edges of the sample were sealed to the glass using epoxy (Loctite 9460). The epoxy was cured at 100 °C in an oven for at least 2 h prior to use. The exposed electrode area was determined by using an optical scanner (Epson perfection V370) and analyzing the image using ImageJ software.

### **Cell preparation and (photo)electrochemical testing:**

All (photo)electrochemical experiments were done in a cell with catholyte and anolyte sides separated by an anion-exchange membrane (AEM), unless otherwise specified. Glass cells were cleaned in aqua regia (4:1 HCl : HNO<sub>3</sub> by volume) and rinsed with deionized water before use. Unless otherwise specified, [Fe(CN)<sub>6</sub>]<sup>3-</sup> and/or KOH were dissolved in deionized water at 10 mM and 1.0 M (pH = 13.6), respectively, and 25 mL of solution was added to the anolyte side. The anolyte was bubbled with O<sub>2</sub> unless otherwise stated. The catholyte side was filled with 1.0 M KOH(aq) and Ni wire was used as the counter electrode. Fumasep (Fuel Cell Store) was used as the AEM to separate the two compartments and prevent crossover of [Fe(CN)<sub>6</sub>]<sup>3-</sup> from reaching the catholyte. Hg/HgO reference electrodes were used for all three-electrode experiments. The reference electrodes were calibrated relative to a reversible hydrogen electrode (RHE), which involved comparing the potential difference between the Hg/HgO electrode and a Pt disk electrode in H<sub>2</sub>-saturated 1.0 M KOH(aq). The potentials of reference electrodes used ranged from 0.904 to 0.918 V vs. RHE. Unless otherwise specified, illumination was provided with an ELH tungsten-halogen lamp through a UV long pass ( $\lambda < 400$  nm) filter and was

calibrated to  $100 \text{ mW cm}^{-2}$  using a calibrated Si photodiode (Thorlabs). Electrochemical measurements were performed using an MPG-2 potentiostat (Bio-Logic Science Instruments).

All current measurements were normalized to current density ( $J$ ) based on the measured electrode area. Ni-coated samples were activated in KOH prior to testing in KOH or KOH and  $[\text{Fe}(\text{CN})_6]^{3-}$  by 20 cyclic voltammetry (CV) cycles between 0.53 V and 1.83 V vs. RHE at  $40 \text{ mV s}^{-1}$ . This activation step has been shown to improve catalytic activity by incorporating Fe from the solution into the catalyst and forming NiFeOOH.<sup>1</sup> Photoelectrodes were subjected to 6 h of illumination under potential control followed by 18 h in the dark at open circuit. A Python script was used to automate turning on and off the lamp at these time intervals followed by 30 s of wait time before starting data collection. For Fig. 1, four electrodes were tested in KOH(aq) with  $[\text{Fe}(\text{CN})_6]^{3-}$  while three electrodes were tested in KOH(aq) alone. Unless otherwise stated, electrodes were held at 1.63 V vs RHE when actively performing water oxidation. For  $\text{np}^+$ -Si photoelectrodes this potential corresponds to the location of the hole quasi Fermi level during  $\text{O}_2$  evolution with this electrocatalyst whereas for dark  $\text{p}^+$ -Si electrodes this potential is sufficient to overcome the catalyst overpotential and evolve  $\text{O}_2(\text{g})$  at a current density of  $\sim 20\text{-}30 \text{ mA cm}^{-2}$ . The actual operating potential in a tandem structure will depend in detail on the overall photovoltage and photocurrent of the system.<sup>2-4</sup> Extensive precedent exists for testing Si electrodes at or near this potential as a representative potential that is slightly positive of, and thus slightly oxidatively stressful relative to, the maximum power point for the photoanode considering the overpotential for the OER electrocatalyst and fill factor losses in the photoelectrode itself.<sup>5-11</sup>

To assess performance of  $\text{np}^+$ -Si/ $\mu\text{Ni}$  photoanodes, the fill factor ( $FF$ ) was calculated using the following equation:

$$FF = \frac{V_{MP}J_{MP}}{V_{OC}J_{SC}}$$

where ( $V_{MP}$ ,  $J_{MP}$ ) is the maximum power point,  $V_{OC}$  is the open-circuit voltage, and  $J_{SC}$  is the current density evaluated at the Nernstian potential of the redox couple of interest in the cell.

Faradaic efficiency measurements were based on a previously published procedure.<sup>12</sup> Briefly, a p<sup>+</sup>-Si sample coated with ~100 nm of Ni was submerged in the anolyte (KOH or KOH and [Fe(CN)<sub>6</sub>]<sup>3-</sup>) in a two-electrode experiment with an inverted burette over the sample. The Ni counter electrode in the KOH catholyte was separated from the other compartment by a Fumasep membrane. A galvanostatic current of 40 mA cm<sup>-2</sup> was applied and the volume of O<sub>2</sub> collected was measured by the inverted burette. 40 mA cm<sup>-2</sup> represents an achievable current density with Si photoanodes that is just below the theoretical maximum of Si (43.3 mA cm<sup>-2</sup>) expected under illumination of a Si photoanode with 100 mW cm<sup>-2</sup> of the AM 1.5G solar spectrum.<sup>13, 14</sup>

### **Etch Rate Experiment:**

A thermal oxide was grown at 950 °C on (100)- and (111)-oriented p<sup>+</sup>-Si for 6 h and 4.5 h, respectively. Ellipsometry measurements indicated an oxide thicknesses of 170-180 nm. After thermal oxide growth, an array of 10 μm by 100 μm rectangles was patterned by standard photolithography procedures. The patterned wafers were then submerged in BOE for 3 min to ensure that all exposed oxide was etched, leaving behind trenches that went down to bare Si surfaces. The wafers were then sonicated in acetone to remove the photoresist. Samples were introduced to either 1.0 M KOH(aq) or 1.0 M KOH(aq) and 10 mM [Fe(CN)<sub>6</sub>]<sup>3-</sup> electrolytes in the dark at open circuit. After the samples were allowed to etch for a set amount of time, the samples were submerged in BOE for 5 min to remove all oxide. For atomic-force microscopy (AFM) measurements, the samples were affixed to a stainless steel disk using carbon tape.

The resulting height difference between the exposed Si and the Si layer protected by the thermal oxide was quantified with AFM (Bruker Dimension Icon). Peak Force Tapping mode was used to collect the data, which tracked the surface topography by relying on a feedback based on the maximum force between the probe and sample for each tapping cycle. The Peak Force amplitude and frequency were set to 100 nm and 2 kHz, respectively, and a ScanAsyst-Air probe (Bruker) with a nominal tip radius of 2 nm was used.

### **Materials Characterization:**

A FEI Nova NanoSEM 450 was used to take scanning electron micrographs (SEMs). The SEMs were measured at a working distance of 5.0 mm and accelerating voltages of 10 kV. Photoelectrodes after testing were prepared by removing the epoxy with a razor blade and cleaving through the center. Each of the two cleaved pieces were affixed to either side of a 45° SEM mount with carbon tape, to examine the surface topography as well as the cross section of the sample.

UV-vis spectroscopy was performed on an Agilent 8453 spectrometer. The 10 mM  $[\text{Fe}(\text{CN})_6]^{3-}$  and 1.0 M KOH(aq) electrolyte was illuminated under nominally the same conditions as the photoelectrode. The electrolyte was diluted 1 : 10 with deionized water before taking measurements. A series of standard solutions with 0.10 M KOH(aq) and either 0.33 mM, 0.5 mM, 0.67 mM or 1 mM  $[\text{Fe}(\text{CN})_6]^{3-}$  was also prepared by weighing the amount on a scale and dissolving in deionized water. The concentrations of  $[\text{Fe}(\text{CN})_6]^{3-}$  and  $[\text{Fe}(\text{CN})_6]^{4-}$  were also measured by fitting the 420 nm ( $A_{420}$ ) and 260 nm ( $A_{260}$ ) absorbance peaks to the following correlation<sup>15</sup>

$$A_{420} = 1.058[Fe(CN)_6^{3-}] - 0.003[Fe(CN)_6^{4-}]$$

$$A_{260} = 1.260[Fe(CN)_6^{3-}] + 2.724[Fe(CN)_6^{4-}].$$

X-ray photoelectron spectroscopy (XPS) was performed using a Kratos Axis Ultra system with a base pressure of  $1 \times 10^{-9}$  Torr in the analysis chamber. A monochromatic Al K $\alpha$  source was used to irradiate the sample with X-rays (1486.7 eV) at 450 W. A hemispherical analyzer oriented for detection along the sample surface normal was used for maximum depth sensitivity. High-resolution spectra were acquired at a resolution of 25 meV with a pass energy of 10 eV. The data were analyzed using CasaXPS computer software. First, the spectra were calibrated by referencing the C 1s peak position to 284.8 eV. Si 2p, Fe 2p, N 1s, O 1s peaks were then fitted to multiple subspecies each having Gaussian-Lorentz peak shapes. XPS data were obtained ex-situ i.e., after a short sample transfer through air, which could potentially confound linking the surface composition and oxidation states found in UHV to the ones involved during electrocatalysis.

### **Estimate of Current Passed for SiO<sub>x</sub> Dissolution and Residual [Fe(CN)<sub>6</sub>]<sup>4-</sup> Oxidation**

We additionally evaluated the behavior in the dark to directly compare water oxidation to oxidation of residual [Fe(CN)<sub>6</sub>]<sup>4-</sup>. The amount of charge passed over time (in C h<sup>-1</sup>) was estimated as follows. We assumed that the electrode area was 0.62 cm<sup>2</sup>, that SiO<sub>x</sub> equates to SiO<sub>2</sub> ( $\rho = 2.65$  g/cm<sup>3</sup>) for this estimate, and that the rate of charge passed was proportional to the etching of an anodic oxide in 1.0 M KOH(aq) and 10 mM [Fe(CN)<sub>6</sub>]<sup>3-</sup> ( $2.7 \times 10^{-7}$  cm/h<sup>-1</sup>).

$$\text{Current} = \left( \left( 2.7 * 10^{-7} \frac{\text{cm}}{\text{h}} \right) * \left( 3600 \frac{\text{sec}}{\text{h}} \right) \left( \frac{2.65 \frac{\text{g SiO}_2}{\text{cm}^3}}{60.08 \frac{\text{g SiO}_2}{\text{mol}}} * 6.022 * 10^{23} \text{ mol}^{-1} \right) \right. \\ \left. * \left( 4e^- * 1.602 * 10^{-19} \frac{\text{C}}{e^-} \right) \right) = 1.3 * 10^{-6} \frac{\text{A}}{\text{cm}^2}$$

Analogously, for an etch rate of  $1.8 * 10^{-7} \text{ cm h}^{-1}$ , the current density is  $0.85 \mu\text{A cm}^{-2}$  and the rate of  $[\text{Fe}(\text{CN})_6]^{3-}$  consumed in the dark was estimated as follows:

$$[\text{Fe}(\text{CN})_6]^{3-} \text{ consumed} = \left( \frac{0.85 * 10^{-6} \frac{\text{C}}{\text{s cm}^2}}{1.602 * 10^{-19} \frac{\text{C}}{e^-}} \right) * \left( \frac{1 [\text{Fe}(\text{CN})_6]^{3-}}{1 e^-} \right) * \left( \frac{1 \text{ mol } [\text{Fe}(\text{CN})_6]^{3-}}{6.022 * 10^{23} [\text{Fe}(\text{CN})_6]^{3-}} \right) \\ = 8.8 * 10^{-12} \frac{\text{mol}}{\text{s cm}^2}$$

Assuming that the  $\sim 30 \text{ mA cm}^{-2}$  of photocurrent density observed in Fig. 1 contributes solely to  $\text{O}_2$  evolution, the rate of  $\text{O}_2$  generated was estimated as follows:

$$\text{O}_2(\text{g}) \text{ generated} = \left( \frac{0.030 \frac{\text{C}}{\text{s cm}^2}}{1.602 * 10^{-19} \frac{\text{C}}{e^-}} \right) * \left( \frac{1 \text{ O}_2}{4 e^-} \right) * \left( \frac{1 \text{ mol O}_2}{6.022 * 10^{23} \text{ O}_2} \right) = 7.8 * 10^{-8} \frac{\text{mol}}{\text{s cm}^2}$$

To assess the impact of  $[\text{Fe}(\text{CN})_6]^{4-}$  oxidation on Faradaic efficiency, the ratio of  $[\text{Fe}(\text{CN})_6]^{4-}$  generated in the dark and  $\text{O}_2$  produced under illumination is described as follows:

$$\text{O}_2 : [\text{Fe}(\text{CN})_6]^{4-} \text{ ratio} = \left( \frac{7.8 * 10^{-8} \frac{\text{mol O}_2}{\text{s cm}^2}}{8.8 * 10^{-12} \frac{\text{mol } [\text{Fe}(\text{CN})_6]^{3-}}{\text{s cm}^2}} \right) * \left( \frac{1 \text{ mol } [\text{Fe}(\text{CN})_6]^{3-} \text{ consumed}}{1 \text{ mol } [\text{Fe}(\text{CN})_6]^{4-} \text{ generated}} \right) \\ = 8.8 * 10^3$$

Thus 88 h of  $[\text{Fe}(\text{CN})_6]^{4-}$  generation in the dark would be required to produce 1% of the amount of  $\text{O}_2(\text{g})$  generated in 1 h under illumination. Assuming no other substantial source of

$[\text{Fe}(\text{CN})_6]^{4-}$ , the impact of  $[\text{Fe}(\text{CN})_6]^{4-}$  is therefore expected to minimally impact the efficiency. This estimate supports the observed Faradaic efficiency displayed in Fig. 4b.

### Supplementary Information Figures

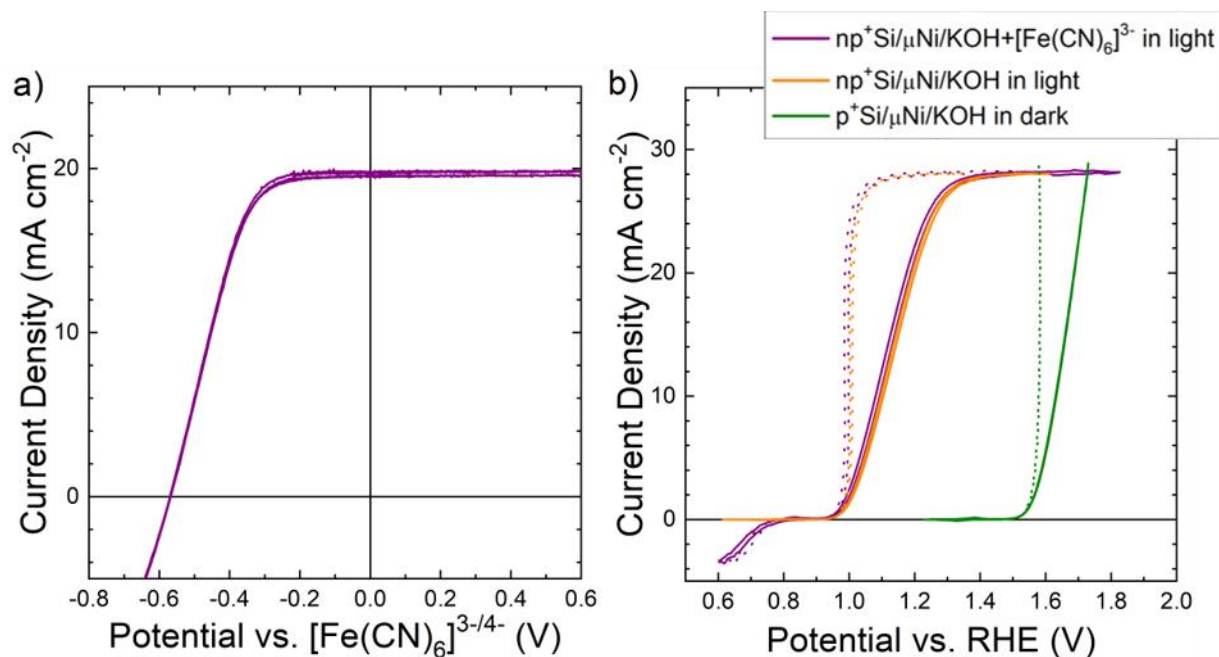


**Figure S1.** Cyclic voltammograms of  $p^+$ - or  $np^+$ -Si(100)/ $\mu\text{Ni}$  electrodes in either dark or under  $100 \text{ mW cm}^{-2}$  illumination, respectively. (a)  $np^+$ -Si(100)/ $\mu\text{Ni}$  in contact with the  $[\text{Fe}(\text{CN})_6]^{3-/4-}$  redox couple ( $0.35 \text{ M } [\text{Fe}(\text{CN})]^{3-}$ ,  $0.050 \text{ M } [\text{Fe}(\text{CN})_6]^{4-}$ , and  $0.50 \text{ M KCl(aq)}$ ). No long-pass filter was used, and the open-circuit voltage is  $570 \text{ mV}$ . (b)  $np^+$ -Si(100)/ $\mu\text{Ni}$  in contact with  $1.0 \text{ M KOH(aq)}$  and  $10 \text{ mM } [\text{Fe}(\text{CN})_6]^{3-}$  (purple) or  $1.0 \text{ M KOH(aq)}$  (orange);  $p^+$ -Si(100)/ $\mu\text{Ni}$  in contact with  $1.0 \text{ M KOH(aq)}$  (green). Measured data (solid lines) were adjusted by subtracting series resistance (dashed lines) to estimate the photovoltage ( $580 \text{ mV}$ ). The scan rate for the cyclic voltammograms was  $40 \text{ mV s}^{-1}$ .

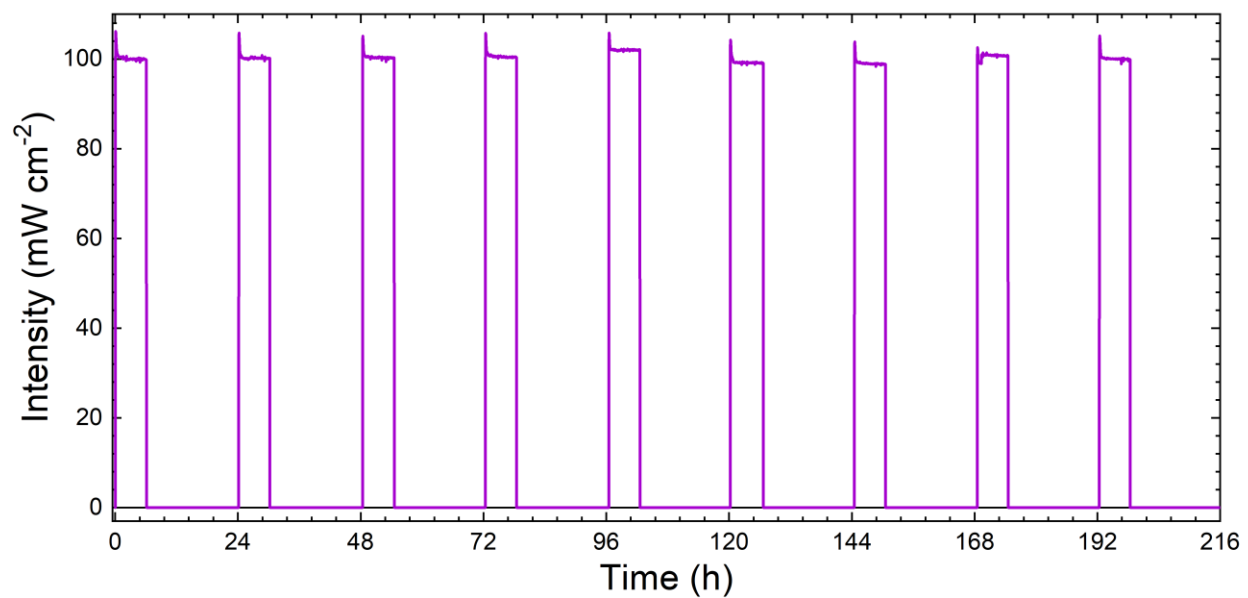


**Figure S2.** Representative light intensity as a function of time used for stability tests with simulated day/night cycles. A calibrated photodiode monitored the illumination from a Xe arc lamp with an AM 1.5 filter.

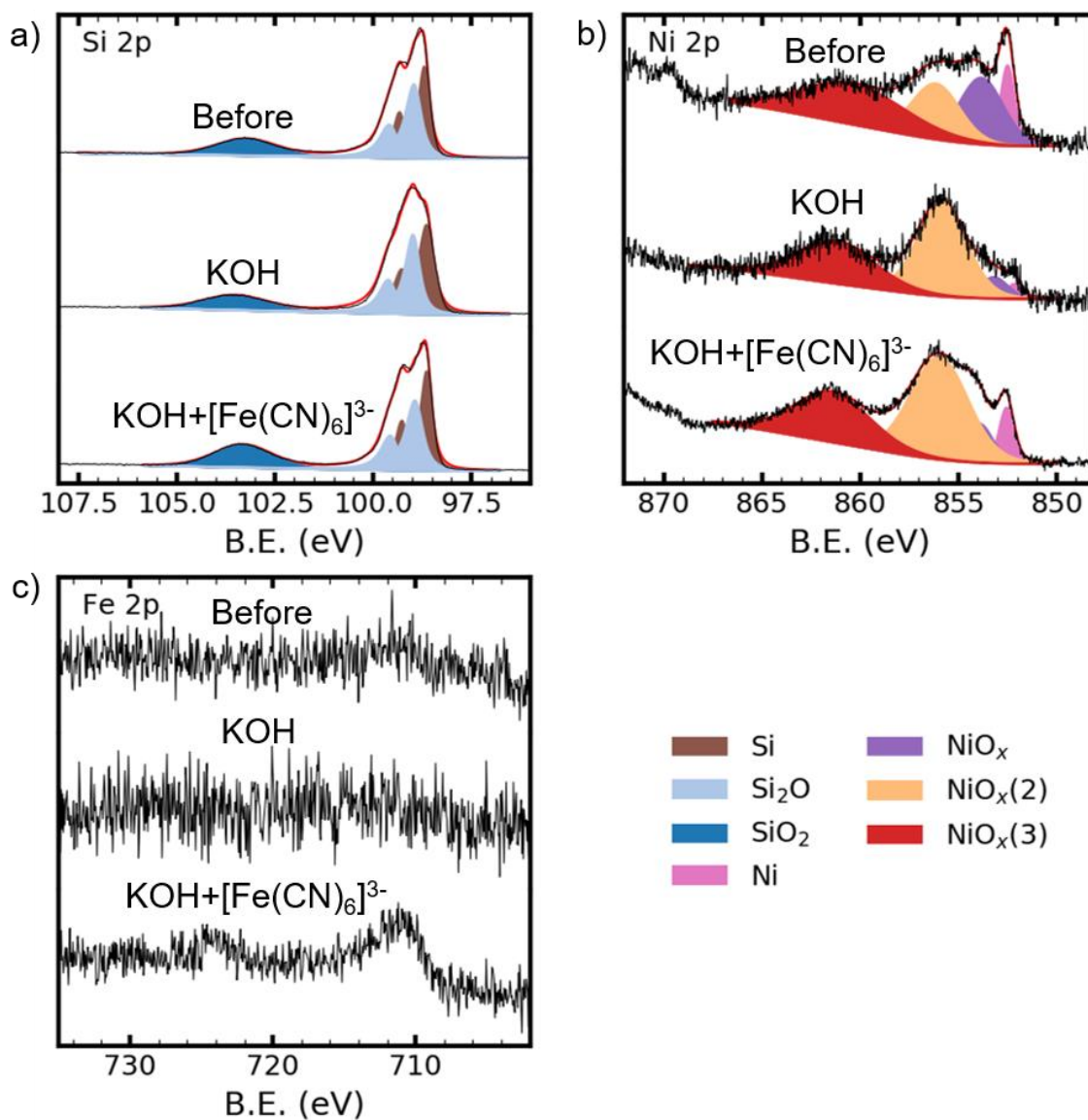


**Figure S3.** High-resolution XPS data of  $\text{np}^+\text{-Si}/\mu\text{Ni}$  photoelectrodes in the (a) Si 2p, (b) Ni 2p, (c) Fe 2p regions. For each element, the top spectrum was obtained before simulated day/night cycling of the illumination, whereas the other spectra were obtained after 6 h under illumination at 1.63 V vs RHE, followed by 18 h at open circuit in the dark, in 1.0 M KOH(aq) (middle) and in the protective electrolyte (bottom). The y-axis is in arbitrary units.

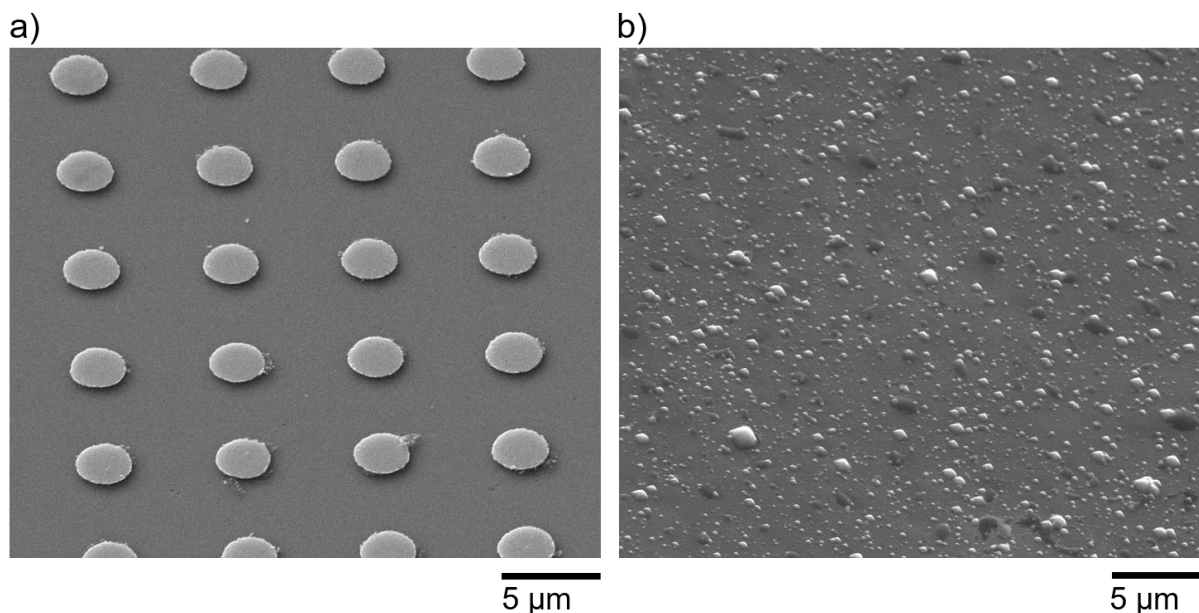


**Figure S4.** Scanning-electron micrographs comparing  $np^+$ -Si/ $\mu$ Ni etching in 1.0 M KOH(aq) with (a) and without (b) bubbling  $O_2$  for 24 h in the dark at open circuit.

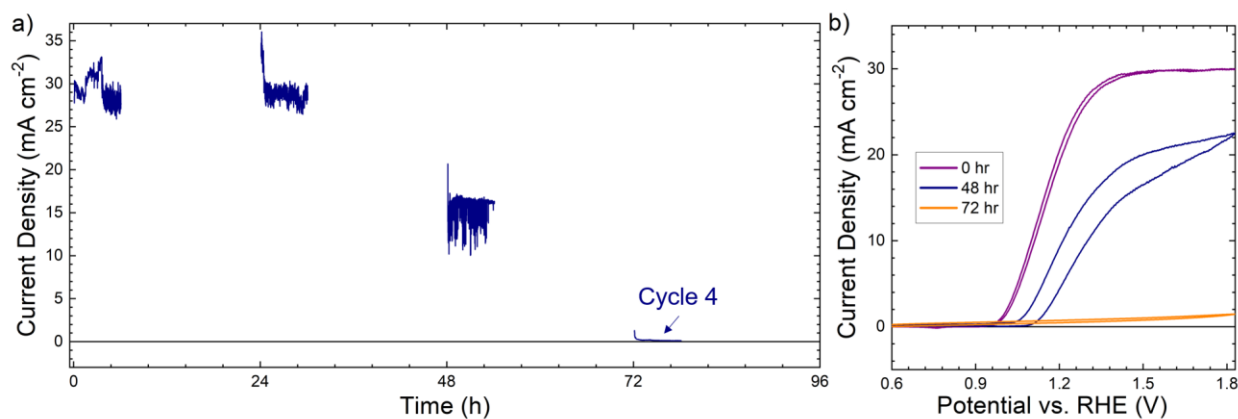


**Figure S5.** Chronoamperometric stability and performance of  $np^+$ -Si(100)/ $\mu$ Ni electrodes in 1.0 M KOH(aq) without  $O_2$  bubbling. (a) Chronoamperometric data were taken in 6 h intervals at 1.63 V vs RHE under  $100 \text{ mW cm}^{-2}$  of illumination, followed by 18 h in the dark at open circuit. (b) Current density vs potential behavior in 1.0 M KOH(aq) at a scan rate of  $100 \text{ mV s}^{-1}$ .

The purpose of testing the stability of  $\text{np}^+\text{-Si}(100)/\mu\text{Ni}$  in KOH without  $\text{O}_2$  bubbling was to illustrate that the saturated  $\text{O}_2$  in solution from the evolved  $\text{O}_2(\text{g})$  during the day cycle was not sufficient to stabilize the electrode during the night cycle during which the solution loses its saturation of  $\text{O}_2$  (Fig. S5).

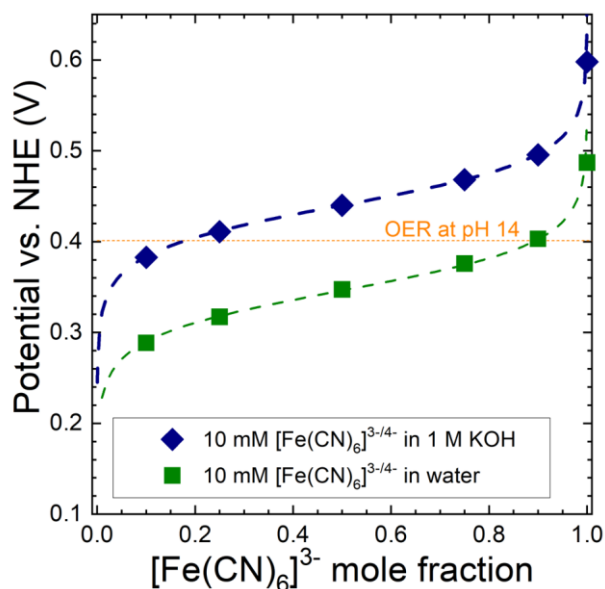


**Figure S6.** Nernst potentials of 10 mM  $[\text{Fe}(\text{CN})_6]^{3-/4-}$  solutions. The measured data points were based on open-circuit potentials of a Pt working electrode at different mole fractions of  $[\text{Fe}(\text{CN})_6]^{3-}$  to  $[\text{Fe}(\text{CN})_6]^{4-}$  in 1.0 M KOH(aq) (blue) or deionized  $\text{H}_2\text{O}$  (green). The dashed blue and green lines were calculated using the Nernst Equation. The dashed orange line represents the potential versus NHE of the OER at pH 14.

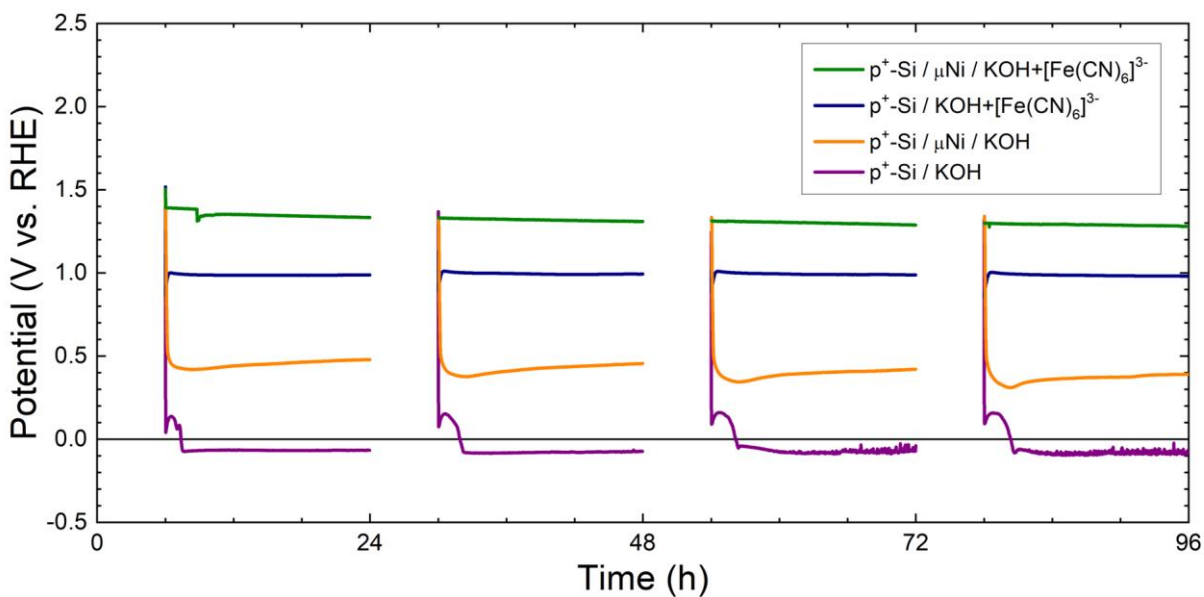


**Figure S7.** Open-circuit potential of p<sup>+</sup>-Si electrodes and of p<sup>+</sup>-Si electrodes coated with μNi, respectively, in contact with 1.0 M KOH(aq) or 1.0 M KOH(aq) with 10 mM [Fe(CN)<sub>6</sub>]<sup>3-</sup>. The gaps in collected data indicate intervals during which the electrode was held at 1.579 V vs RHE. The purpose of this experiment was to evaluate the potential at which the surface equilibrated in the dark. Si does not photocorrode under these conditions,<sup>17, 18</sup> so the  $E_{OC}$  for the photoactive material is not directly relevant to the issue being addressed experimentally.

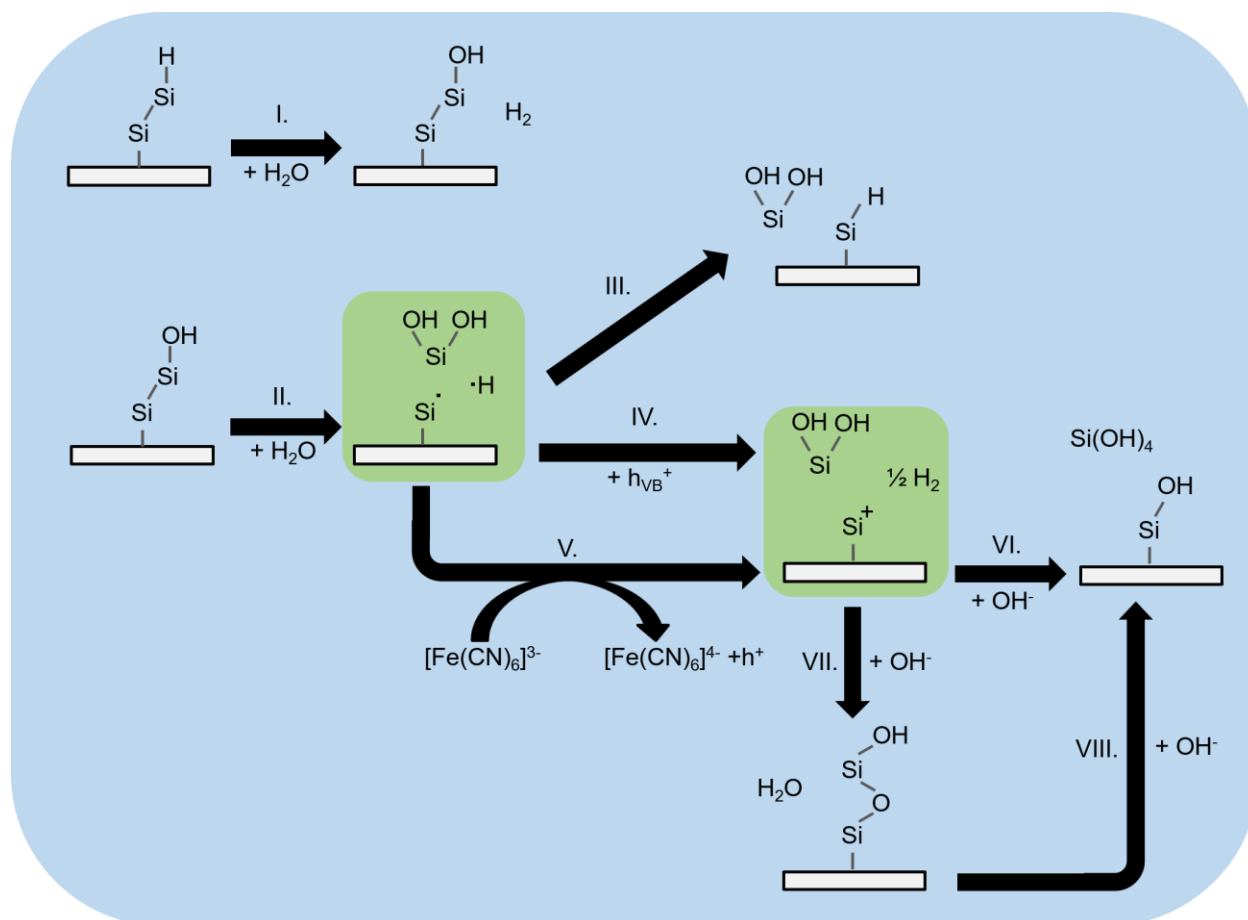


**Figure S8.** Schematic for possible surface reactions of Si in basic electrolyte.<sup>16</sup> The reaction intermediates are found within the green boxes. In the dark at open circuit, the intermediate product from reaction II undergoes either reaction III in KOH or reaction V in KOH and  $[\text{Fe}(\text{CN})_6]^{3-}$ . Under positive bias, this intermediate can undergo reaction IV. Holes from either reactions IV or V contribute to formation of oxide layer via reaction VII. The sample dissolution rate slows if reactions VIII or VI occur instead of reaction III.

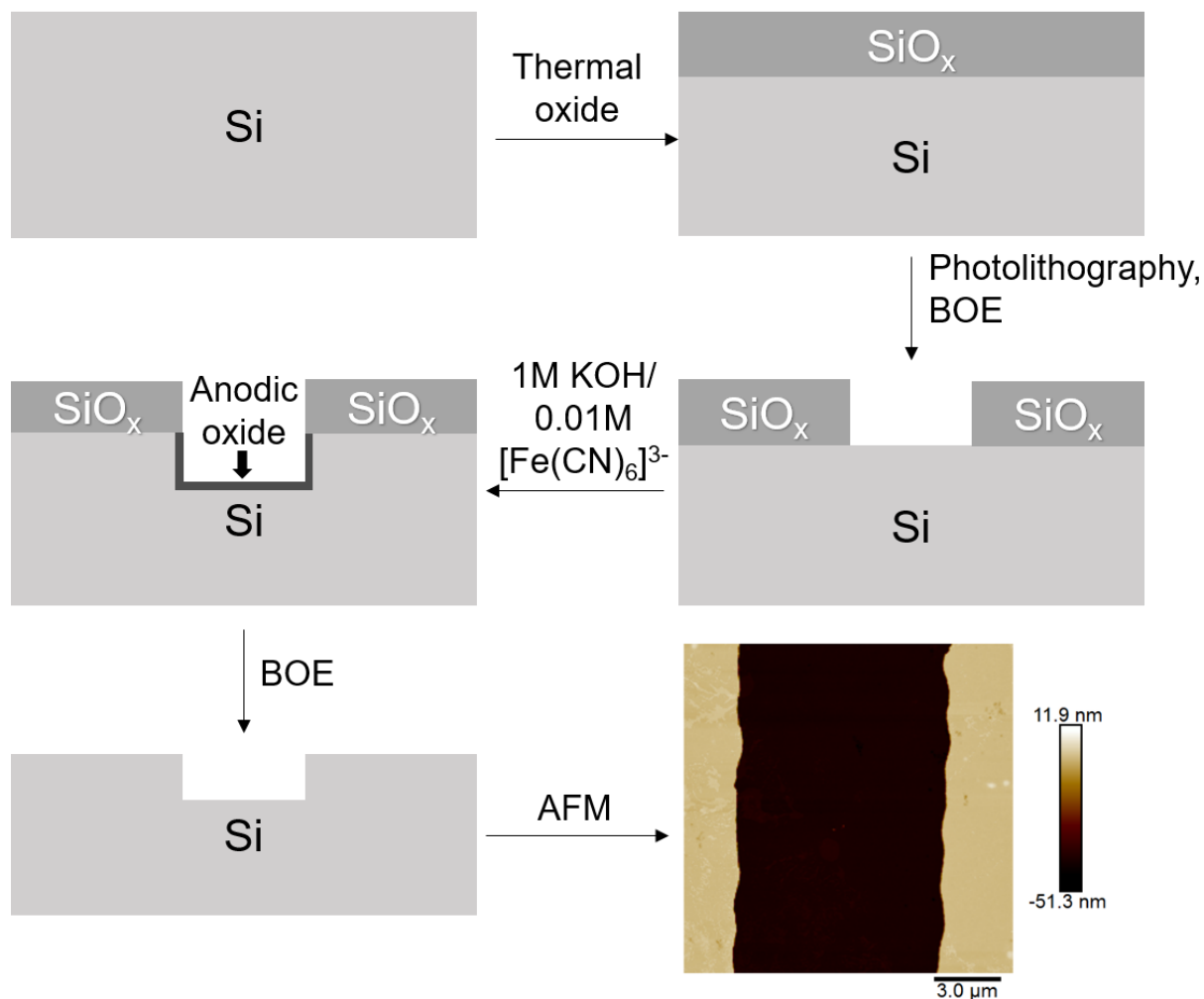


**Figure S9.** Schematic of the experiment to determine the etch rate of the passivating oxide. The final step depicts a representative AFM image of a p<sup>+</sup>-Si(100) surface after etching in 1.0 M KOH(aq) and 10 mM [Fe(CN)<sub>6</sub>]<sup>3-</sup> for 24 h at open circuit.

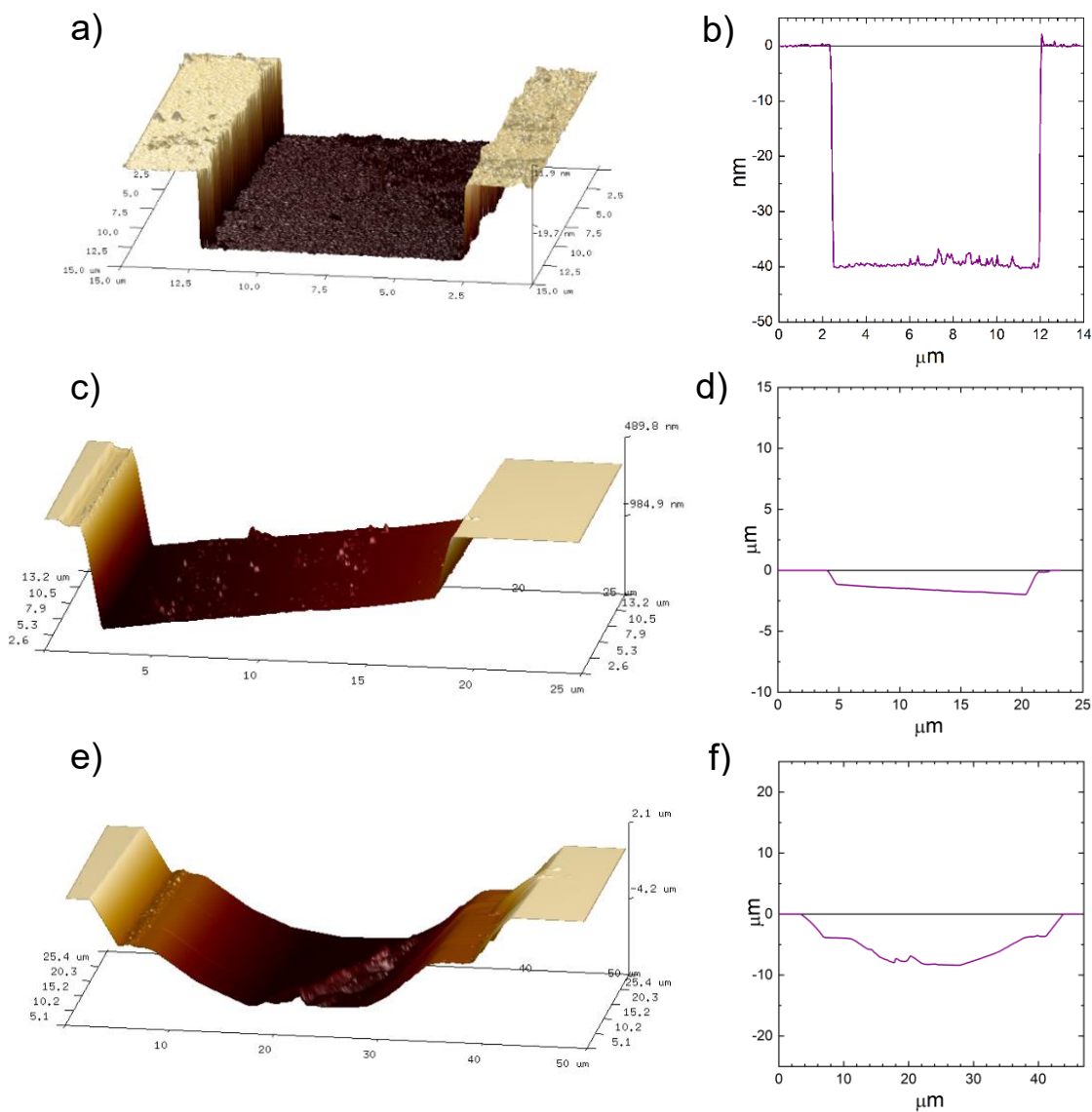


**Figure S10.** Topography of Si trenches after etching. (a-b) 3D profile of a Si(100) trench and corresponding cross sectional height profile after 24 h in 10 mM  $[\text{Fe}(\text{CN})_6]^{3-}$  and 1.0 M KOH(aq). (c-d) 3D profile of a Si(111) trench and height profile after 24 h in 1.0 M KOH(aq). The base of the etch pit is angled  $\sim 3^\circ$  off the normal axis, suggesting that Si(111) is exposed when the miscut angle of the wafer is taken into account. (e-f) 3D profile of a Si(100) trench and height profile after 24 h in 1.0 M KOH(aq). The etch pit morphology is dependent on a combination of mask undercutting and exposure of the (111) facet. The top edge of the etch pit is angled at  $\sim 53^\circ$ , close to the expected angle between Si(111) and Si(100).

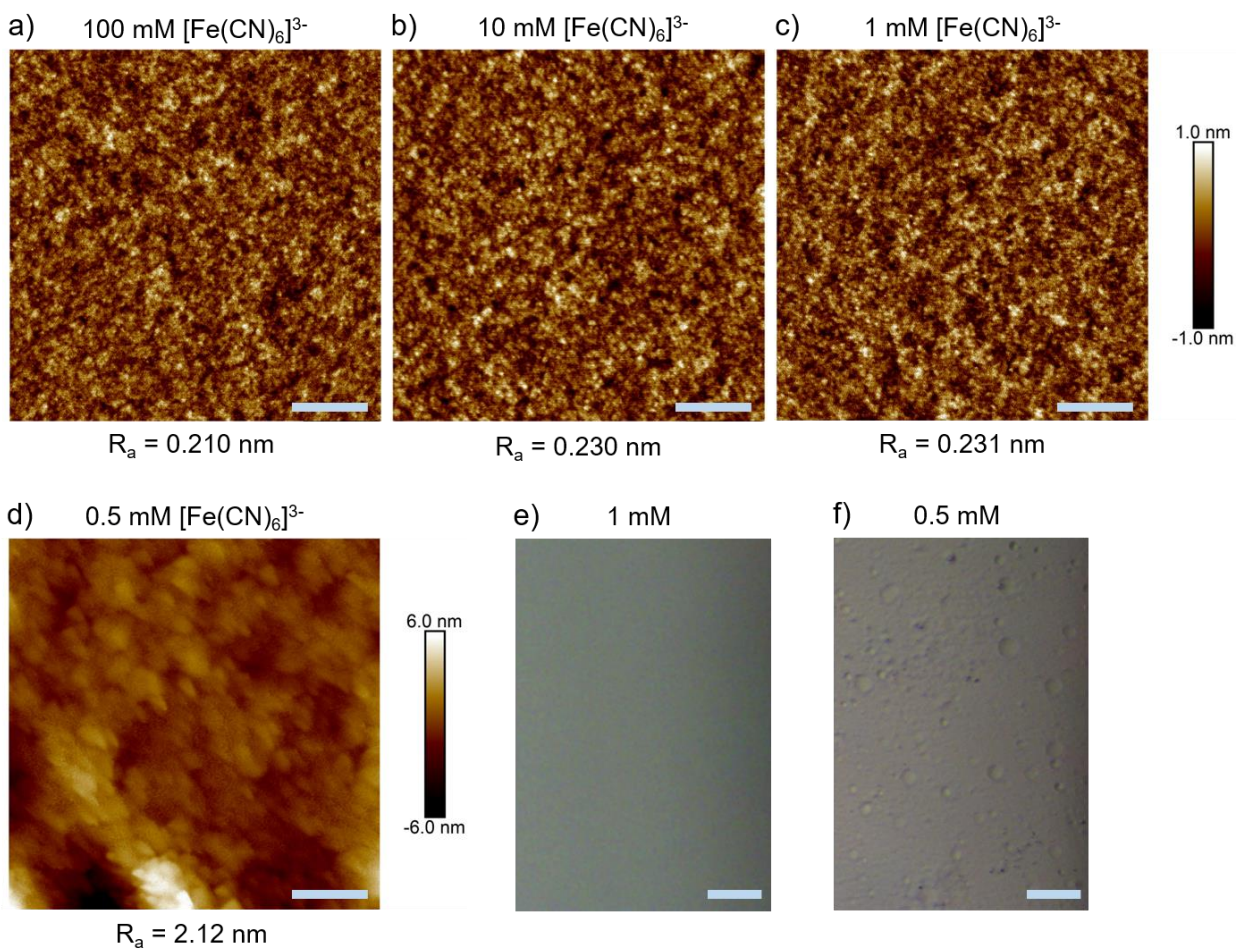


**Figure S11.** Atomic force microscope (a-d) and optical images (e-f) of  $p^+$ -Si(100) after 18 h at open circuit in 1.0 M KOH(aq) and (a) 100 mM, (b) 10 mM, (c,e) 1 mM, or (d,f) 0.5 mM  $[\text{Fe}(\text{CN})_6]^{3-}$ . The surface roughness ( $R_a$ ) was calculated sampling multiple scans at random points on 3 samples for each condition. The scale bar represents 200 nm for (a-d) and 20  $\mu\text{m}$  for (e-f).

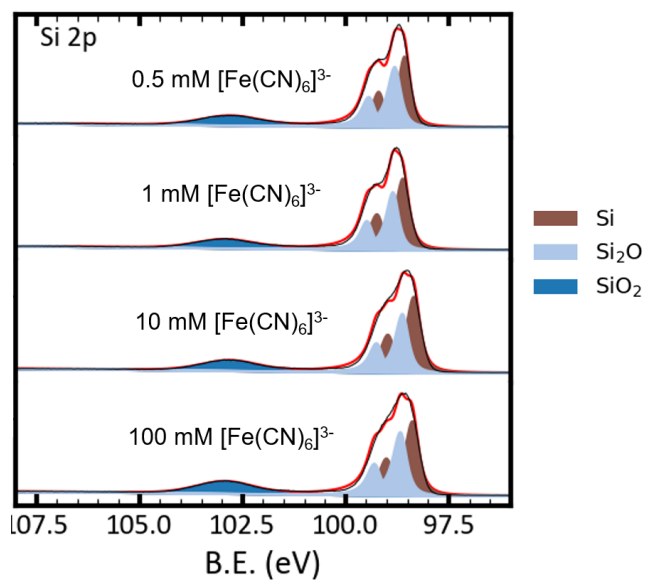


**Figure S12.** High-resolution XPS data in the Si 2p region of  $\text{p}^+\text{-Si}(100)$  after 18 h at open circuit in 1.0 M  $\text{KOH}(\text{aq})$  and 0.5 mM, 1 mM, 10 mM, or 100 mM  $[\text{Fe}(\text{CN})_6]^{3-}$ . The y-axis is in arbitrary units.

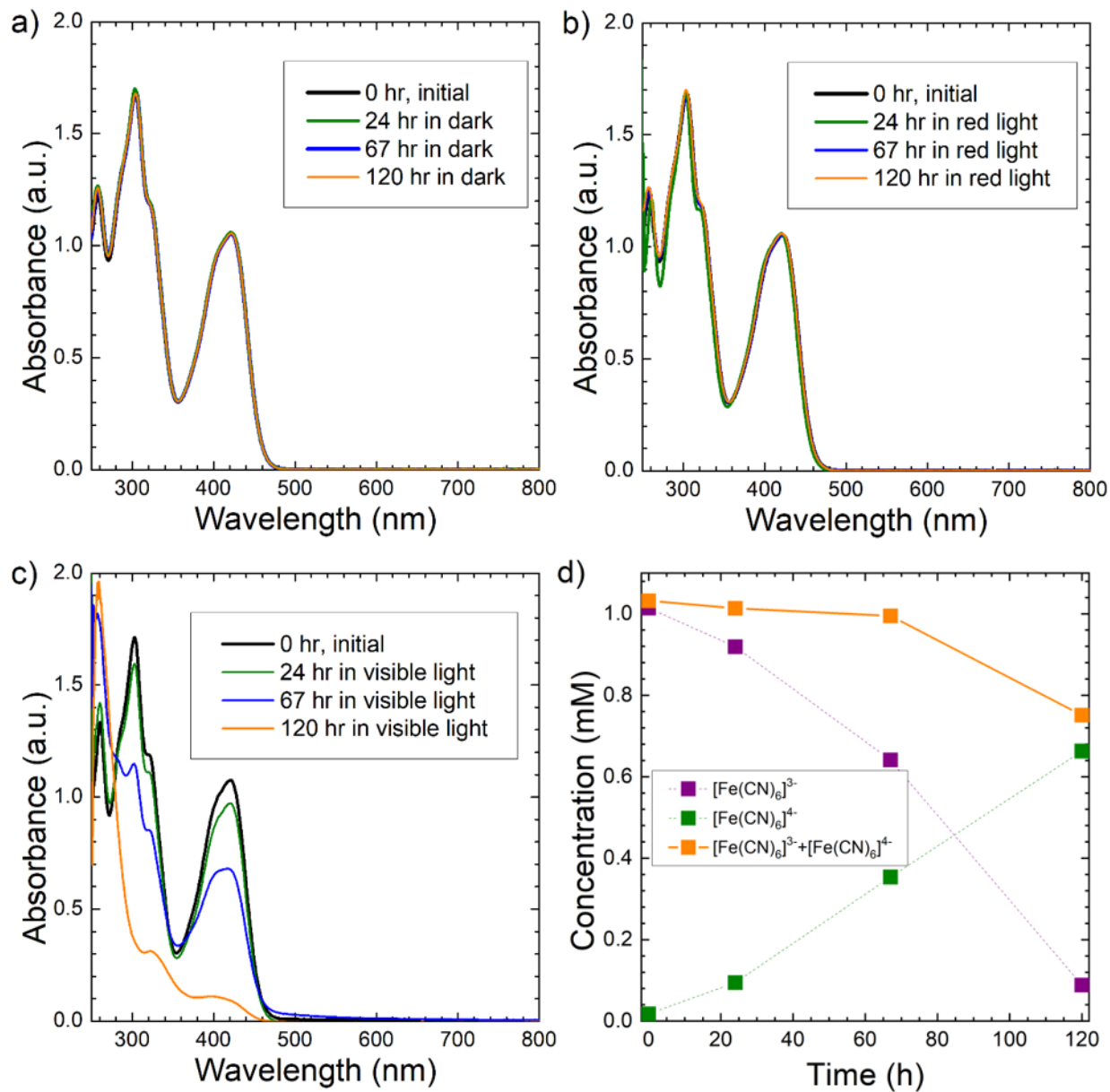


**Figure S13.**  $[\text{Fe}(\text{CN})_6]^{3-/4-}$  UV-vis spectra and concentrations under different illumination conditions. UV-vis spectra of  $1 \text{ mM } [\text{Fe}(\text{CN})_6]^{3-}$  in  $0.1 \text{ M KOH}(\text{aq})$  at 0, 24, 67, and 120 h under (a) dark, (b) 627 nm LED, and (c) ELH lamp illumination with a 400 nm long pass filter. (d)  $[\text{Fe}(\text{CN})_6]^{3-/4-}$  concentrations under visible light obtained from fitting the 420 nm and 260 nm peaks in (c).

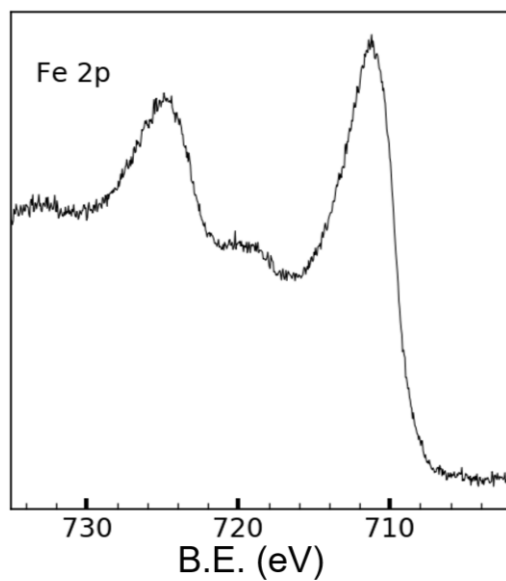


**Figure S14.** High-resolution XPS data in the Fe 2p region of the precipitate produced by shining visible light on 10 mM  $[\text{Fe}(\text{CN})_6]^{3-}$  in 1.0 M KOH(aq). The y-axis is in arbitrary units.

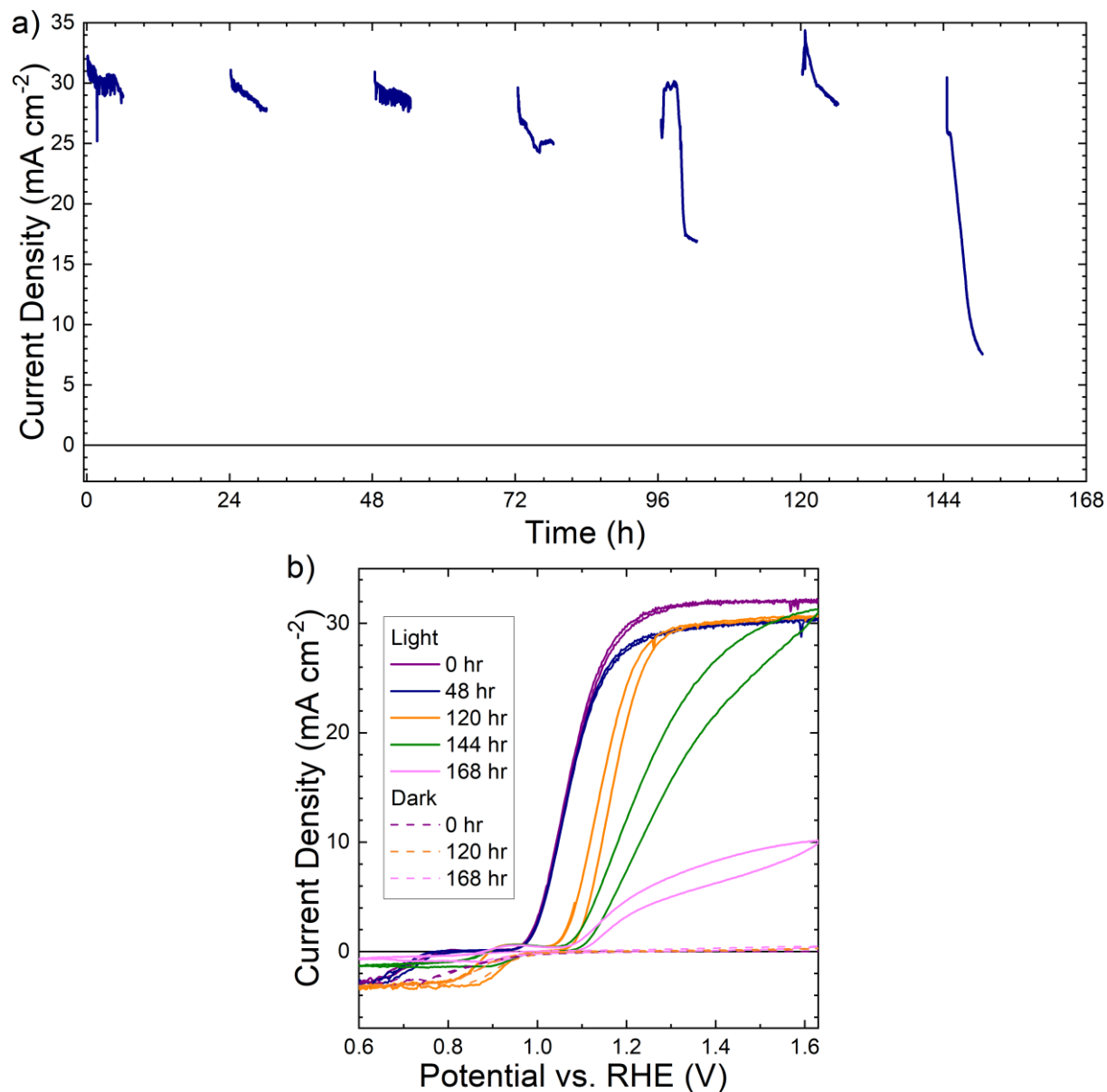


**Figure S15.** Stability and performance of an  $np^+$ -Si(100)/ $\mu$ Ni electrode in 1.0 M KOH(aq) and 10 mM  $[\text{Fe}(\text{CN})_6]^{3-}$  with  $100 \text{ mW cm}^{-2}$  of illumination provided by a Xe arc lamp with an AM 1.5 filter. (a) Chronoamperometric data were taken in 6 h intervals at 1.63 V vs RHE under illumination, followed by 18 h in the dark at open circuit. The electrolyte was replaced and  $\text{O}_2(\text{g})$  was bubbled for  $\sim 5$  min at the end of each 24 h period. (b) Current density vs potential behavior at a scan rate of  $40 \text{ mV s}^{-1}$  under illumination (solid lines) and in the dark (dashed lines).

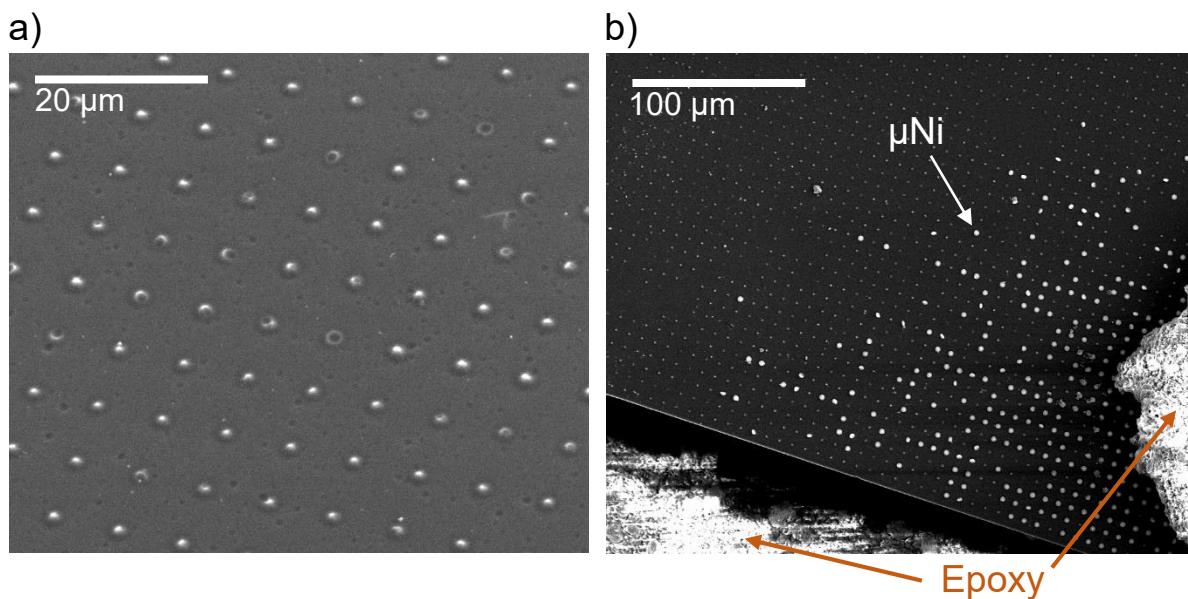


**Figure S16.** Scanning-electron micrographs of  $np^+$ -Si(100)/ $\mu$ Ni electrodes after testing for 169 h. (a) Center of the electrode where  $\mu$ Ni was predominantly delaminated. (b) The corner of the electrode surrounded by epoxy, where  $\mu$ Ni was mostly intact.

As discussed in the text, these Fig. S13 and S14 suggest that the eventual failure that the electrode experienced is mechanical, rather than photochemical. Moreover,  $[\text{Fe}(\text{CN}_6)]^{3-}$  decomposition can be circumvented when a tandem device is used, as described in the main text. There is thus no evidence of wavelength-dependent corrosion due to hot holes at the current density tested for Si in alkaline media. Other reports have also used solar simulators with AM 1.5 filters and have shown that n-Si/Ni nanoparticle photoanodes are stable and do not exhibit Si photocorrosion under these conditions.<sup>17, 18</sup>

Additionally,  $\text{O}_2(\text{g})$  was only bubbled for  $\sim 5$  min each day right before acquiring the cyclic voltammetry data. Although not a 1:1 comparison with Fig. 1 due to the use of a Xe lamp without a UV filter, the  $\text{SiO}_x$  corrosion behavior remained consistent whether or not the solution was saturated with  $\text{O}_2$  for the duration held at open circuit.

**Table S1.** Fill factors of np<sup>+</sup>-Si(100)/μNi photoanodes

Corresponding Figure	Electrolyte <sup>a</sup>	Hours tested (h)	Fill factor <sup>b</sup>	$J_{sc}^b$ (mA cm <sup>-2</sup> )	$V_{oc}^b$ (V)
1b	[Fe(CN) <sub>6</sub> ] <sup>3-</sup> , KOH, O <sub>2</sub> sat.	0	0.40±0.02	27±2	0.58±0.02
1b	[Fe(CN) <sub>6</sub> ] <sup>3-</sup> , KOH, O <sub>2</sub> sat.	48	0.38±0.02	27±2	0.59±0.02
1b	[Fe(CN) <sub>6</sub> ] <sup>3-</sup> , KOH, O <sub>2</sub> sat.	120	0.40±0.02	28±1	0.58±0.02
1b	[Fe(CN) <sub>6</sub> ] <sup>3-</sup> , KOH, O <sub>2</sub> sat.	216	0.35±0.05	28±1	0.55±0.04
1b	[Fe(CN) <sub>6</sub> ] <sup>3-</sup> , KOH, O <sub>2</sub> sat.	288	0.34	28	0.55
1c	KOH, O <sub>2</sub> sat.	0	0.37±0.04	29±2	0.58±0.02
1c	KOH, O <sub>2</sub> sat.	48	0.27	29	0.59
1c	KOH, O <sub>2</sub> sat.	120	N/A <sup>c</sup>	N/A <sup>c</sup>	N/A <sup>c</sup>
S4b	KOH	0	0.35	30	0.57
S4b	KOH	48	0.18	21	0.52
S4b	KOH	72	N/A <sup>c</sup>	N/A <sup>c</sup>	N/A <sup>c</sup>

<sup>a</sup>[Fe(CN)<sub>6</sub>]<sup>3-</sup> concentration is 10 mM; KOH concentration is 1.0 M

<sup>b</sup>Error bars indicate multiple samples tested for each time indicated

<sup>c</sup>Electrode experienced complete failure

**Table S2.** Etch rates of Si under various experimental conditions

[Fe(CN) <sub>6</sub> ] <sup>3-</sup> concentration (mM)	KOH concentration (M)	p <sup>+</sup> -Si orientation	Potential (V vs. RHE)	Etch rate (nm h <sup>-1</sup> )
0	1.0	(100)	$E_{oc}$	330±20
0	1.0	(111)	$E_{oc}$	84±6
10	1.0	(100)	$E_{oc}$	1.8±0.1
10	1.0	(111)	$E_{oc}$	1.7±0.1
0	1.0	(100)	1.63	2.7±0.1
10	1.0	(100)	1.63	2.9±0.1
100	1.0	(100)	$E_{oc}$	2.1±0.1
50	1.0	(100)	$E_{oc}$	1.9±0.1
1	1.0	(100)	$E_{oc}$	1.4±0.1
0.5	1.0	(100)	$E_{oc}$	1.2±0.1
0.1	1.0	(100)	$E_{oc}$	380±20

## References

1. L. Trotochaud, S. L. Young, J. K. Ranney and S. W. Boettcher, *Journal of the American Chemical Society*, 2014, **136**, 6744-6753.
2. M. G. Walter, E. L. Warren, J. R. McKone, S. W. Boettcher, Q. Mi, E. A. Santori and N. S. Lewis, *Chemical Reviews*, 2010, **110**, 6446-6473.
3. Y. Chen, S. Hu, C. Xiang and N. S. Lewis, *Energy & Environmental Science*, 2015, **8**, 876-886.
4. S. Hu, C. Xiang, S. Haussener, A. D. Berger and N. S. Lewis, *Energy & Environmental Science*, 2013, **6**, 2984-2993.
5. I. A. Moreno-Hernandez, B. S. Brunshwig and N. S. Lewis, *Advanced Energy Materials*, 2018, **8**, 1801155.
6. K. Sun, F. H. Saadi, M. F. Lichterman, W. G. Hale, H. P. Wang, X. Zhou, N. T. Plymale, S. T. Omelchenko, J. H. He, K. M. Papadantonakis, B. S. Brunshwig and N. S. Lewis, *Proc Natl Acad Sci U S A*, 2015, **112**, 3612-3617.
7. X. Zhou, R. Liu, K. Sun, K. M. Papadantonakis, B. S. Brunshwig and N. S. Lewis, *Energy & Environmental Science*, 2016, **9**, 892-897.
8. Y. W. Chen, J. D. Prange, S. Dühnen, Y. Park, M. Gunji, C. E. D. Chidsey and P. C. McIntyre, *Nature Materials*, 2011, **10**, 539.
9. M. R. Shaner, S. Hu, K. Sun and N. S. Lewis, *Energy & Environmental Science*, 2015, **8**, 203-207.
10. X. Zhou, R. Liu, K. Sun, D. Friedrich, M. T. McDowell, F. Yang, S. T. Omelchenko, F. H. Saadi, A. C. Nielander, S. Yalamanchili, K. M. Papadantonakis, B. S. Brunshwig and N. S. Lewis, *Energy & Environmental Science*, 2015, **8**, 2644-2649.
11. K. Sun, M. T. McDowell, A. C. Nielander, S. Hu, M. R. Shaner, F. Yang, B. S. Brunshwig and N. S. Lewis, *The Journal of Physical Chemistry Letters*, 2015, **6**, 592-598.
12. K. Sun, Nicole L. Ritzert, J. John, H. Tan, W. G. Hale, J. Jiang, I. Moreno-Hernandez, K. M. Papadantonakis, T. P. Moffat, B. S. Brunshwig and N. S. Lewis, *Sustainable Energy & Fuels*, 2018, **2**, 983-998.
13. P. K. Nayak, J. Bisquert and D. Cahen, *Advanced Materials*, 2011, **23**, 2870-2876.
14. I. A. Moreno-Hernandez, S. Yalamanchili, H. J. Fu, H. A. Atwater, B. S. Brunshwig and N. S. Lewis, *Journal of Materials Chemistry A*, 2020, **8**, 9292-9301.
15. M. Chakrabarti and E. Roberts, *Journal of the Chemical Society of Pakistan*, 2008, **30**, 817-823.
16. X. H. Xia and J. J. Kelly, *Electrochimica Acta*, 2000, **45**, 4645-4653.
17. G. Loget, B. Fabre, S. Fryars, C. Mériadec and S. Ababou-Girard, *ACS Energy Letters*, 2017, **2**, 569-573.
18. S. A. Lee, T. H. Lee, C. Kim, M. G. Lee, M.-J. Choi, H. Park, S. Choi, J. Oh and H. W. Jang, *ACS Catalysis*, 2018, **8**, 7261-7269.